

# Halo Clustering Bias or how well dark matter halos trace the large scale distribution

M. Manera<sup>1</sup> & E. Gaztañaga<sup>2</sup>

<sup>1</sup>Center for Cosmology and Particle Physics, New York University, 4 Washington Place, NY 10003, New York, USA

<sup>2</sup>Institut de Ciències de l'Espai, CSIC/IEEC, Campus UAB, F. de Ciències, Torre C5 par-2, Barcelona 08193, Spain

18 July 2022

## ABSTRACT

Does light trace the mass? The generic answer is: NO. We thus need to understand how this could bias the clustering statistics we infer from data using different tracers. A first step to understand this is to study how dark matter halos, which host galaxies, trace the dark matter distribution. In this paper we explore the biasing in the clustering statistics of halos in simulations. We do so by looking at the two and three point correlation functions at large scales, as well as at the variance and skewness of one of the big (intermediate) simulations run by the MICE consortium. We find that we can predict the large scale halo clustering to better than 10% precision using the local (non-linear) biasing model and peak-background split anstaz. We also test directly the local bias prescription  $T = f(\delta)$  between the mass fluctuations,  $\delta$ , and its trace,  $T$ . We find the local linear,  $b_1$ , and quadratic,  $c_2$ , biasing parameters by fitting the  $f(\delta)$  scattered relation directly from the halo-mass measurements in the simulation. These biases are then compared with the corresponding biases inferred from clustering measurements and with the peak-background split prediction, from the measured mass function. Differences in the  $b_1$  and  $c_2$  estimates can be as large as 10%. We find that most of the discrepancy between the values of  $b_1$  from the halo variance and from fitting the local relation can be attributed to the next to leading order terms in the local bias expansion and to the scatter contribution towards the variance. We show that modeling the shot-noise with Poisson statistics overcorrects the contribution from the scatter in the local relation. Finally, because there is a discrepancy between the peak-background split predictions and the clustering bias, we find 5-10% systematic (and similar statistical) errors in the halo mass estimation out of these bias measurements. Although this is a potential warning for dark energy experiments, these systematics effects can in principle be calibrated using simulations.

## 1 INTRODUCTION

In the new era of precision cosmology it becomes crucial to understand accurately how the spatial distribution of galaxies is related to the underlying dark matter distribution. This relation, which is called galaxy bias, due to the fact that galaxies are known to form in dark matter halos, can be approached in two natural steps. The first step is the bias between halos and dark matter. The second step is the bias between galaxies and halos, which is commonly approached by means of models of galaxy occupation in halos (see for instance Zheng et al 2005 & 2009, Brown 2008, Tinker 2006 & 2009) In this paper we will address the first one. We will study the clustering of dark matter halos in a big cosmological dark matter simulation from the MICE collaboration. The results of this paper are relevant for halo surveys like the South Pole Telescope (SPT); galaxy surveys

like the Sloan Digital Sky Survey (SDSS), the Dark Energy Survey (DES), or SDSS-III (BOSS); and any other survey that traces the large scale the halo or matter distribution.

A simple model for the halo bias, introduced by Fry and Gaztañaga (1993), is to assume a general non-linear (but local and deterministic) relation between the density contrast in the distribution of halos and the density contrast of the dark matter, i.e.,  $\delta_h = F[\delta_m]$ . This is the local halo bias model and it is an approximation. In reality, the bias is stochastic and not deterministic, (see Dekel & Lahav 1999 for modeling) and at some level, due to tidal forces, it will have non-local contributions. It is also not clear to what extend the halo or galaxy density should depend on the underlying matter density only, without including other direct dependencies (like the gravitational potential, for instance). Here we want to study the halo clustering and to address how well the local bias model performs. The failure of the local bias

model could point towards what other contributions should be included next (if any) when analysing observational data to the precision needed for the current generation of surveys.

In this paper we will work with the comoving data from the MICE intermediate simulation which has a volume of  $V = (1536 Mpc/h)^3$ . The use of simulations to study the structure formation and clustering is well motivated as they allow to separate the different physical contributions that combine in an observation as well as to estimate systematics and statistical errors. Also, since we have both dark matter and halo data, we can directly fit the local bias relation from the simulation and compare this results to the large scale bias that we find from clustering measurements like the variance, the skewness or large scale two and three point correlations functions. With the volume we have we can measure the correlation function to the Baryon Acoustic Oscillation (BAO) scales and look for hints of scale dependence. In this work we will use comoving outputs at two redshifts  $z = 0$  and  $z = 0.5$ .

Under few assumptions that go under the name of peak background split anstaz, one can predict the local bias parameters from the mass function of halos. This prediction will test locality and also the assumption that the conditional mass function of an overdense (underdense) patch of the universe can be treated as it were equal to the average mass function of the universe at a different time, or mean density. Peak background split predictions for the bias, specially from a Seth Tormen mass function (Sheth and Tormen 1999), has been used a lot in the literature. In this paper we will compare these bias predictions with the bias from clustering, and study their dependence on the halo mass threshold used to fit the mass function. The inaccuracy of the peak background split has also been studied in Manera, Sheth and Scoccimarro (2010) with complementary results to those of work.

The relation between the mass function and the bias can be inverted; consequently one may use the bias as a proxy for the mass of the halo sample. Systematic errors in estimating the mass from the bias would propagate to and broaden the constraints on cosmological parameters like the equation of state parameter,  $w$  when deduced from the halo mass function. Notice that self calibration methods for the mass function, which are expected to be used by DES-like surveys, assume a known mass bias relation (Lima & Hu 2008, 2009). In this work we will assess how well the halo mass is recovered by using as input the clustering bias parameters from the two and from the three point correlation functions.

The paper is organized as follows. In section II we introduce the clustering statistics we are going to use as well as the local bias model. In section III we present the MICE simulation that we will use in the paper. In section IV we deal with the halo mass function of the simulation and its fits at different mass thresholds. In Section V we obtain the local bias from the direct measurement of the scatterplot relations and show its dependency on the smoothing scale. In this section we also compare the local bias measurements with the peak backgrounds split predictions for halos. In section VI we add to the comparison the bias of obtained from the variance and the skewness and comment

on second order contributions to their differences. In section VII we study the two point correlation and in section VIII the three point correlation. We compare the bias parameters we get in those two sections from that from predictions and variance measurements. In section IX we discuss how well we can recover the mass of halos from the bias parameters. We present our conclusions in section X.

## 2 CORRELATION FUNCTIONS AND BIASING

The two and three-point correlation functions are defined, respectively, as (Bernardeau et. al. 2002)

$$\xi(r_{12}) = \langle \delta(r_1)\delta(r_2) \rangle \quad (1)$$

$$\zeta(r_{12}, r_{23}, r_{13}) = \langle \delta(r_1)\delta(r_2)\delta(r_3) \rangle \quad (2)$$

where  $\delta(r)$  is the local density contrast at position  $r$  smoothed over a given characteristic  $R$  scale. The expectation value is taken over different realizations of the cosmological model. In practice, we apply the ergodic theorem and perform the average over different spatial positions in our universe, which are assumed to be a fair sample of possible realizations (Peebles 1980). As a particular case, when the two or three points are in fact the same ( $r_1 = r_2 = r_3$ ), we get the variance and the skewness. They are defined as

$$\sigma^2 = \langle \delta^2 \rangle = \frac{1}{N} \sum_{i=1}^N \delta_i^2 \quad (3)$$

$$m_3 = \langle \delta^3 \rangle = \frac{1}{N} \sum_{i=1}^N \delta_i^3 \quad (4)$$

where the sum (allowed due to the ergodic theorem) is over a fair sample of points in the simulation. In this case, one typically considers these quantities as a function of the smoothing radius  $R$ , while the correlation functions are displayed as a function of pair separation  $r_{12}$ . In the limit  $r_{12} \gg R$  correlations are independent of  $R$ , while for  $r_{12} \simeq R$  both measurements are closely related.

It is also convenient to define the normalized skewness and the hierarchical  $Q_3$  parameter as follows (Growth & Peebles 1977)

$$S_3 = \frac{m_3}{\sigma^4} \quad (5)$$

$$Q_3 = \frac{\zeta(r_{12}, r_{23}, r_{13})}{\zeta_H(r_{12}, r_{23}, r_{13})} \quad (6)$$

$$\zeta_H \equiv \xi(r_{12})\xi(r_{23}) + \xi(r_{12})\xi(r_{13}) + \xi(r_{23})\xi(r_{13}), \quad (7)$$

where we have introduced a definition for the "hierarchical" three-point function  $\zeta_H$ . Based on early galaxy measurements of  $\zeta$ , the  $Q_3$  parameter was thought to be roughly constant as a function of triangle shape and scale (see Peebles 1980), a result that is usually referred to as the hierarchical scaling. It was later shown (see Peebles 1980, Fry 1984) that one expects deviations from this scaling due to gravitational clustering, which creates filamentary structure (eg see the review of Bernardeau et al 2002).

To describe the three parameters that define the  $\zeta$  or

$Q_3$  triangle, it has been customary to use the two sides of the triangle  $r_{12}$  and  $r_{23}$  (which are typically comparable in size) and the angle  $\alpha$  between them:

$$\cos(\alpha) = \frac{\vec{r}_{12} \cdot \vec{r}_{23}}{r_{12} r_{23}} \quad (8)$$

with  $0 < \alpha < 180$  deg.

The  $Q_3$  parameter has been measured in surveys (Feldman et. al. 2001; Gaztanaga et. al. 2005) and in simulations (Scoccimarro et al. 1999; Barriga & Gaztanaga 2002; Gaztanaga & Scoccimarro 2005). It shows a characteristic *U-shape* (see figures 21 and 22) which results from gravitational instability: elongated triangles have larger probabilities because of the gravitational collapse. In the initial Gaussian field  $\zeta$ ,  $Q_3$  and  $S_3$  are all zero.

## 2.1 The local halo bias model

A simple model for halo or galaxy bias was introduced by Fry and Gaztanaga (1993). These authors assumed that the density contrast in the halos (or galaxy) distribution  $\delta_h$  can be expressed as a general non-linear function of the local density contrast of dark matter,  $\delta_m$ , so that:  $\delta_h = F[\delta_m]$ . On large enough scales, where the fluctuations in the density field are smoothed so that the matter density contrast is of order unity or smaller, this relation can be expanded in a Taylor series

$$\delta_h = \sum_{k=0}^{\infty} \frac{b_k}{k!} \delta_m^k = b_0 + b_1 \delta_m + \frac{b_2}{2} \delta_m^2 + \dots \quad (9)$$

where the  $k = 0$  term comes from the requirement that  $\langle \delta_h \rangle = 0$ . Within this local bias model, at scales where  $\xi_2 < 1$ , we can write the biased (halo or galaxy) two and three point functions to the leading order in  $\xi$  (Fry & Gaztanaga 1993; Frieman & Gaztanaga 1994) as

$$\begin{aligned} \xi^h(r) &\simeq b_1^2 \xi(r) \\ Q_3^h &\simeq \frac{1}{b_1} (Q_3 + c_2) \end{aligned} \quad (10)$$

where  $c_2 \equiv b_2/b_1$ , and the  $\simeq$  sign indicates that this is the leading order contribution in the expansion given by equation 9 above. We can also write the halo skewness as:

$$S_3^h = \frac{1}{b_1} (S_3 + 3c_2) \quad (11)$$

Thus, we can see that, in general, even when  $\delta_m \ll 1$ , the linear bias prescription is not accurate for higher-order moments, (i.e.,  $Q_3$ ), the reason being that nonlinearities in bias (i.e.  $c_2$ ) generate non-Gaussianities of the same order as those of gravitational origin.

The linear bias term  $b_1$  can produce distortions in the shape of  $Q_3$ , while the non-linear bias terms  $c_2$  only shifts the curve. Because  $b_1$  typically increases with the halo or cluster mass, the U-shape of  $Q_3$  as a function of  $\alpha$  is typically suppressed, resulting in a more hierarchical form of the 3-point function  $\zeta \simeq \zeta_H$ . Therefore, it is possible to use the shape of  $Q_3^h$  in simulations (or observations) to separate  $b_1$  from  $c_2$ . This is done by comparing the dark matter predictions with the simulations (observations) data results

and adjusting the bias parameters. This gives an estimate of the linear bias  $b_1$  which is independent of the overall amplitude of clustering  $\xi$ . This approach has already been implemented for the skewness  $S_3$  (Gaztanaga 1994, Gaztanaga & Frieman 1994), the bispectrum (Frieman & Gaztanaga 1994, Fry 1994, Feldman et al. 2001, Verde et al. 2002) or the angular 3-point function (Frieman & Gaztanaga 1999, Gaztanaga & Scoccimarro 2005, Gaztanaga et al. 2005).

## 2.2 Press-Schechter and Sheth-Tormen halo model predictions

In the peak-background split anstaz (Bardeen et al. 1986; Cole & Kaiser 1989) one can relate the halo bias with the halo mass function at large scales by treating perturbed regions as if they were unperturbed regions in a slightly different background cosmology universe but one of the same age (Martino & Sheth 2009). Consequently, from a well motivated functional form of the mass function, one can derive theoretical predictions for the halo bias parameters as well as study their accuracy (Mo et al. 1996, Scoccimarro et al. 2001, Cooray & Sheth 2002, Manera et al 2010). In this paper we will use the Sheth and Tormen (1999) mass function:

$$n(m)dm = \frac{\rho_m}{m} f(\nu) d\nu \quad (12)$$

$$f(\nu) = A(p) \left(1 + (q\nu)^{-p}\right) \left(\frac{q\nu}{2\pi}\right)^{1/2} \exp\left(-\frac{q\nu}{2}\right) \quad (13)$$

where the normalization is given by

$$A(p) = \left[ 1 + \frac{2^{-p} \Gamma(1/2 - p)}{\sqrt{\pi}} \right]^{-1} \quad (14)$$

With this mass function the bias predictions are

$$\begin{aligned} b_1(m, z) &= 1 + \epsilon_1 + E_1 \\ b_2(m, z) &= 2(1 + a_2)(\epsilon_1 + E_1) + \epsilon_2 + E_2 \end{aligned} \quad (15)$$

where  $a_2 = -17/21$ , and  $\epsilon_1$ ,  $E_1$  and  $E_2$  are

$$\begin{aligned} \epsilon_1 &= \frac{q\nu - 1}{\delta_{sc}(z)} & \epsilon_2 &= \frac{q\nu}{\delta_{sc}(z)} \left( \frac{(q\nu)^2 - 6q\nu + 3}{\delta_{sc}(z)} \right) \\ E_1 &= \frac{2p/\delta_{sc}(z)}{1 + (q\nu)^p} & E_2 &= \frac{1 + 2p}{\delta_{sc}(z)} + 2\epsilon_1 \end{aligned} \quad (16)$$

Throughout the paper  $\nu = \delta_{sc}^2(z)/(D^2(z)\sigma_0^2(m))$ . In this notation  $D(z)$  is the growth factor in units of its value at  $z = 0$ ;  $\sigma_0(m)$  is the linear variance of the matter field at redshift  $z = 0$ , when smoothed with a top hat filter of radius  $R = (3m\bar{\rho}/4\pi)^{-1/3}$  and  $\delta_{sc}(z)$  is the critical density contrast for collapse at a given redshift  $z$ . Although it is popular in the literature to use a fix value for  $\delta_{sc}$  we will be using its proper spherical collapse redshift dependence (Eke et al 1996, Cooray & Sheth 2002) since there is some indications that in this case the mass function closer to universal (Manera et al 2010).

These predictions for the bias depend on the mass function through the parameters  $p$  and  $q$ . When  $p = 0$  and  $q = 1$

we recover the Press-Schechter (Press & Schechter 1974) formula. Original values for the mass function fit were  $p \simeq 0.3$  and  $q \simeq 0.7$  (Sheth & Tormen 1999) which discusses afterwards that  $q = 0.75$  (and therefore  $A \simeq 0.3222$ ) gives better results (Sheth & Tormen 2001; Cooray & Sheth 2002). We confirmed that this is the case and consequently we will use the latter values for the ST fit as their fiducial values in our plots. At the same time we will also use our own set of  $p$  and  $q$  values obtained by fitting the mass function as we explain in section 4. Bias parameters from a mass function fit form like that Warren et al (2006) has been studied by Manera et al (2010) and showed to give similar results than that of ST for a range of masses similar to that of this paper.

The above  $b_i(m)$  predictions are for a given halo mass, while we would like to have predictions for halos above a certain mass  $b_i(m > M)$ , which we will get from simulations. One could relate both estimations by integrating over the mass function:

$$b_i(m > M) = \frac{1}{n_h} \int_{m > M} dm n(m) b_i(m), \quad (17)$$

Also, the halo number density is given by

$$n_h = \int_{m > M} dm n(m) \quad (18)$$

If one have a model for populating galaxies in halos, i.e a halo occupation distribution (HOD) that give the number of galaxies of a given type (i.e., luminosity and color) given the mass of the halo  $< N_g | m >$ , then we can introduce it in equations 17 18 and obtain the galaxy bias. If the bias model works, looking at the observed galaxies would allow us to fit the (usually two) HOD parameters. For an approach of how this can be done with SDSS survey (and also to see the  $b_i$  dependence on mass) see, for instance, Sefusatti & Scoccimarro (2005). Tinker et al 2009 shows also that how a similar HOD fit analysis can be used to understand the red sequence of galaxies.

### 3 THE MICE INTERMEDIATE SIMULATION

We will analyse the halo bias and clustering of the MICE intermediate dark matter simulation from the MICE collaboration<sup>1</sup>. This simulation have been run with Marenostrum at the Barcelona Supercomputer Center using the L-GADGET code, periodic boundary conditions, and 128 processors. Two hundred comoving outputs from  $z = 1.4$  to  $z = 0$  have been produced (12 TBytes of data). In this paper we will use the  $z = 0.0$  and the  $z = 0.5$  outputs. They have  $N = N_{1D}^3 = 1024^3$  dark matter particles over a cubical box of size  $L = 1536 \text{ Mpc}/h$ . This particles have been put in cubic cells of  $4 \text{ Mpc}/h$  producing a density mesh, from which we will compute the correlation functions and the direct local bias. The particle mass resolution of the simulation is

$$M = 27.75 \left( \frac{L}{N_{1D}} \right)^3 \Omega_m 10^{10} M_\odot/h \simeq 2.34 \cdot 10^{11} M_\odot/h \quad (19)$$

<sup>1</sup> For more information about the MICE collaboration team and the simulations run see <http://ice.cat.es/mice/>

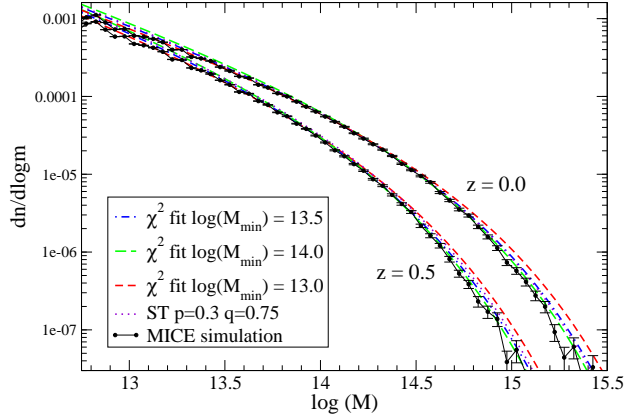


**Figure 1.** Mass function for halos in the MICE simulation at redshifts  $z = 0$  (upper curves) and  $z = 0.5$  (lower curves). Compare them with ST best fits starting at  $\log(M) = 13.0, 13.5$  and  $14.0$ .

The cosmological model parameters for the simulation are  $\Omega_m = 0.25$ ,  $\Omega_\Lambda = 0.75$ ,  $\Omega_B = 0.044$ ,  $n_s = 0.95$ ,  $h = 0.7$  and  $\sigma_8 = 0.8$ . The softening length of the simulation is 50 Kpc/h. The initial conditions were set at  $z = 50$  using Zeldovich approximation.

A list of groups with 20 or more particles is provided on the fly by the Friends of Friends algorithm in the GADGET code. These groups will be our halos, and from them we will compute the halo correlation function and the bias predictions. We have set the linking length to be 0.168 times the mean interparticle distance, which results in 2729833 halos at  $z=0$ , and 2110669 halos at  $z=0.5$ . The effect of changing linking length have been studied in Manera, Sheth and Soccimarro 2010.

By working with comoving data we concentrate on the gravitational evolution and structure formation and get rid of redshift distortions and other lightcone effects, which might not be directly related to the question addressed. Nevertheless, since at the end we want to model observational data, the inclusion of lightcone effects and redshifts distortions have to be considered as the natural next step in our study. In fact lightcone outputs from the MICE simulations have already been produced and stored in a set of all sky maps, which were lately used to study systematics in mass functions derived from lensing (see Fosalba Gaztañaga, Cautin & Manera 2008).

### 4 THE MASS FUNCTION

We have computed the mass function of halos for the MICE simulation and show it in figure 1. Halo masses have been corrected for discreteness effects following Warren et al. (2006). The mass of the halo is set therefore equal to  $M_p N(1 - N^{-0.6})$  where  $N$  is the number of particles and  $M_p$  the particle mass. This correction has been experimen-

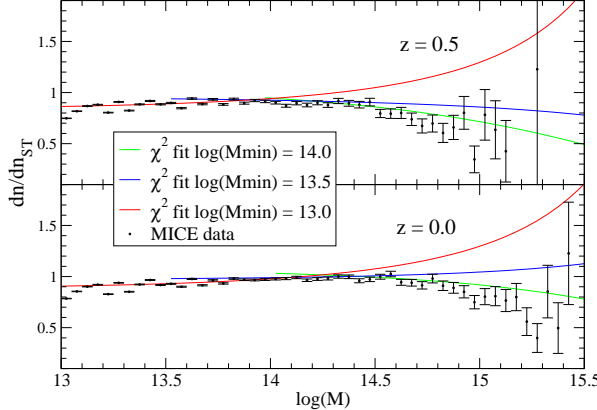


**Figure 2.** Ratios of the MICE mass function fits and data respect Sheth and Thormen mass function with  $p = 0.3$  and  $q = 0.75$ .

tally set using a linking lenght equal to 0.2 times the mean interparticle distance while we are using 0.168. Differences in the correction are very likely to be minimal if not negligible for the halo range in which we fit the mass function. Notice also that Crocce et al. (2009) has tested this correction for MICE simulations by means of randomly removing a fraction of the dark matter particles as a way of lowering the mass resolution, and found it to work quite well.

Starting from different lower mass theresholds for halos we have performed a  $\chi^2$  fit to the mass function data. Best fits for Sheth and Tormen (ST) functional forms are shown as dashed colored lines in figure 1, while data is in blak dots. The fits are dominated by the lower mass bins which have smaller errorbars. For comparison we have added a mass function plot with the commonly used ST fiducial values  $(p, q) = (0.3, 0.75)$ . To apprecciate better the differences between fits we show in figure 2 the ratio of the best fit c urves to that of the ST fiducial case.

$\log(M_{min})$	$z$	$p$	$q$	$\sigma_p$	$\sigma_q$
13.0	0.0	0.334	0.665	0.001	0.003
13.5	0.0	0.309	0.733	0.002	0.004
14.0	0.0	0.275	0.786	0.004	0.006
13.0	0.5	0.347	0.691	0.001	0.003
13.5	0.5	0.312	0.763	0.003	0.004
14.0	0.5	0.280	0.801	0.010	0.011

**Table 1** Best fit values of the Sheth and Tormen's  $p$  and  $q$  paramters to the simulation mass function, and their jack-knife errors  $\sigma_p$  and  $\sigma_q$ .

The values for  $p$  and  $q$  of each fit are shown in the Table 1. Statistical errors come from jack-knife subsampling and are computed in the following way. We divide our simulation in 64 compact regions with equal volume. Then we create a set of  $J = 64$  jack-knife subsamples of the data by removing each time one of these regions from the whole sample. For

each jack-knife subsample we compute the mass function and fit its  $(p, q)$  parameters. Errors in the parameters we are interested, in this case  $p$  and  $q$  but that we name generically as  $\theta$  can be obtained as

$$(\Delta\theta)^2 = \frac{(J-1)}{J} \sum_j (\bar{\theta} - \theta_j)^2 \quad (20)$$

where  $\bar{\theta}$  is the average over the jack-knife subsamples. We also take  $\bar{\theta}$  to be the best fit value. Errors in the mass functions are taken to be poisson but do not change significatively if they are estimated by the jack-knife method as well. Similar results are obtained if we divide the simulation in 27 jack-knife regions instead of 64. We find jack-knife errors on of  $p$  and  $q$  (see table 1) are smaller than the systematic errors that we are trying to asses by setting different halo mass theresholds.

Notice that in section 5.1 we will compute predictions and errors from the bias using the mass function. This is, from the jack-knife set of  $p$  and  $q$  we will compute a set of jack-knife bias applying equation 16, and errors will be given by equation 20.

## 5 BIAS FROM SCATTER IN $\delta_H$ VS $\delta_M$

We are interested in determining the local bias parameters directly. In order to do so we will compare the halo density contrast  $\delta_h$  with the local matter density fluctuation  $\delta_m$  at different cells. This will give an scatter plot of the relation  $\delta_h = F[\delta_m]$ , from which we can obtain  $b_1$  and  $c_2$  by means of a least mean square fit to the local bias parabola (equation 9).

One prominent feature of the scatter plots (see figures 3 and 4) is the discreteness of the  $\delta_h$  values, i.e., that we see horitzontal lines in the figures. This obviously comes from the fact that we have an integer number of halos in each cell. The step in the halo density fluctuations is consequently  $\Delta\delta_h = 1/\bar{n}$ , where  $\bar{n}$  is the mean number of halos in the cells. This is the value of the shot noise, which will decrease when increasing the cell size or when lowering the mass thereshold of halos, for we will have a larger  $\bar{n}$ . Notice that the matter density field is also discrete, but because the large number of matter particles per cell this effect is not visible in the plots.

One issue to be addressed is the dependence of the bias parameters' fit on the size of the cell used to smooth the density field. Figures 3 and 4 show the scatter plots of halos of more than 50 particles when changing the size of the cubical cell along three different values  $l_c = 24, 48, 128$  Mpc/h, which correspond to spherical top hat volumes of radius  $R_s = 14.9, 29.8, 79.4$  Mpc/h as labeled in the figures. Right and left side respectively show results for  $z = 0$  and  $z = 0.5$ . We can see that for the smallest smoothing radius the scatter of points is very big. In this case there are many points with  $\delta_m \geq 1$  which situate us in a regime where the Taylor expansion of  $F[\delta_m]$  can not be applied. When the radius is larger the scatter gets reduced and almost all points have  $\delta_m < 1$ . To get a better idea of the convergence of the fit we

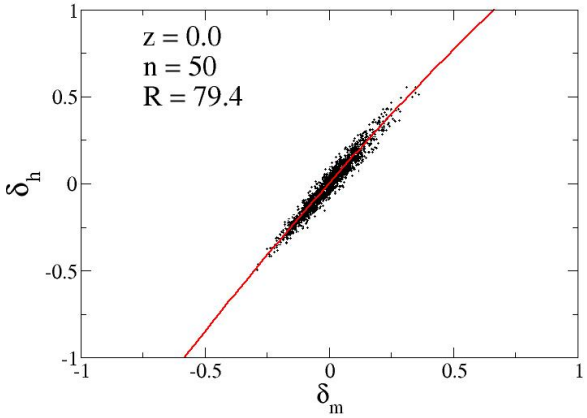
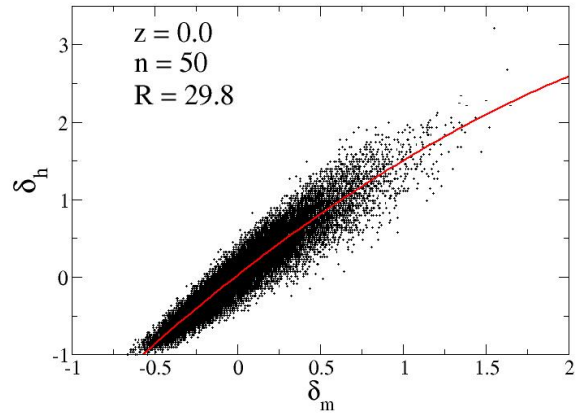
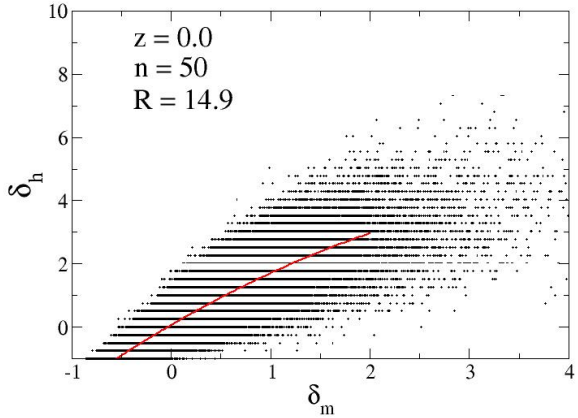


**Figure 3.** Scatter plots showing halo density contrast  $\delta_h$  for halos of 50 or more particles versus dark matter density fluctuations  $\delta_m$ . Results are shown for a different cell sizes with equivalent radius  $R_s$  as labeled in the figure. Results are for simulation data at redshift  $z=0$ . In a continuous line we show the least square fit to the local bias parabola (equation 9)

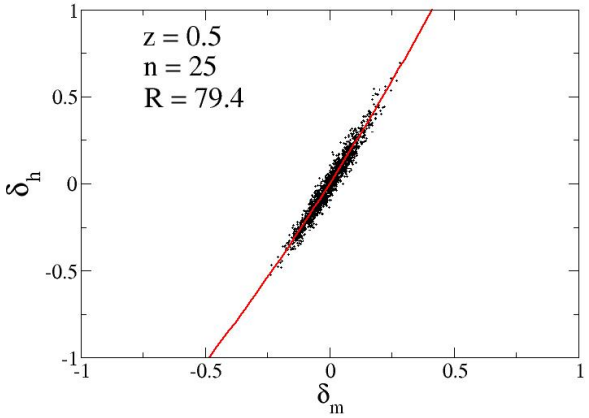
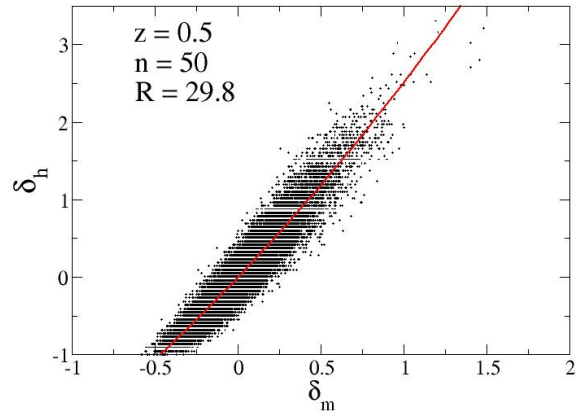
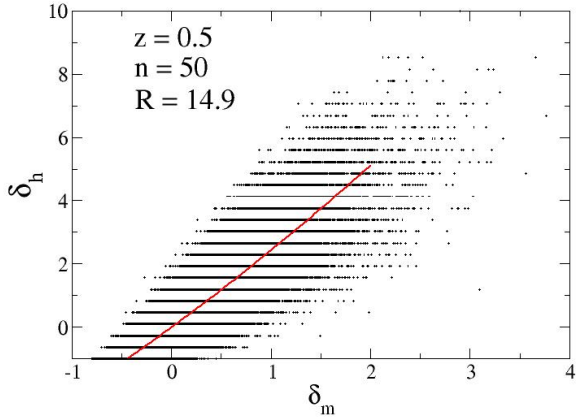


**Figure 4.** Same as Fig 3 at  $z = 0.5$

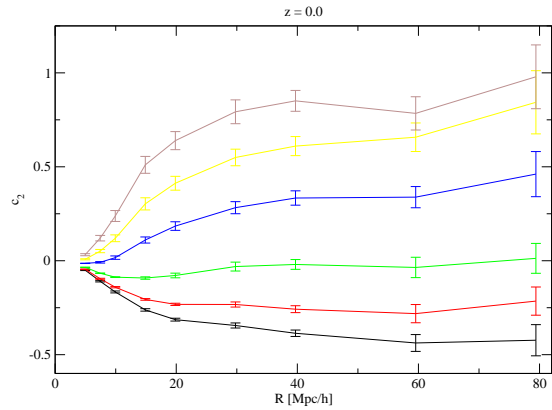
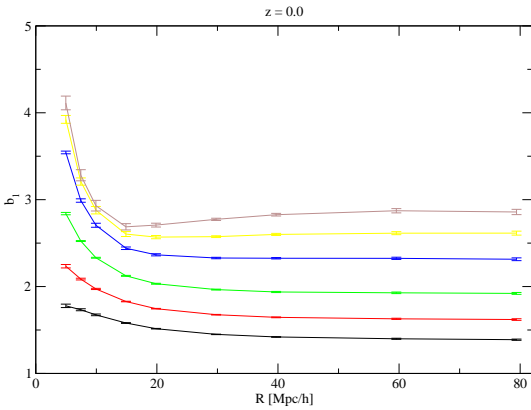
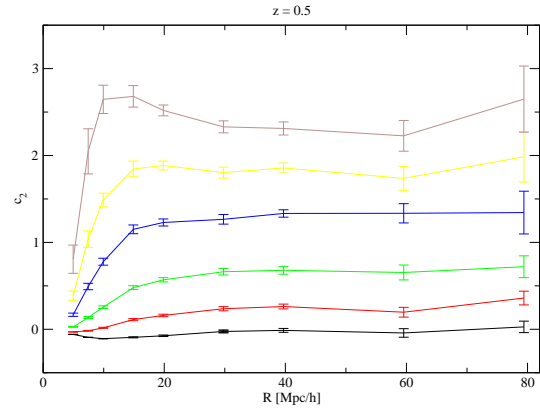
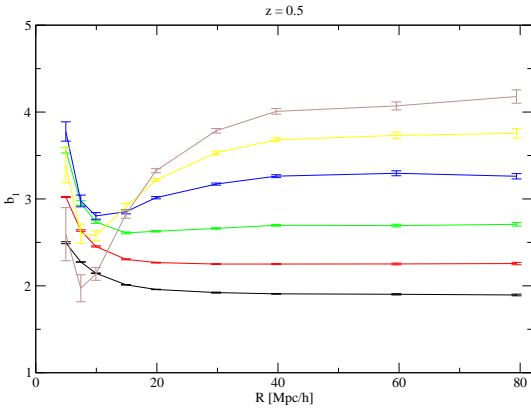


**Figure 5.** Dependence of  $b_1$  on the smoothing radius. Top panel corresponds to  $z = 0.5$  and bottom panel to  $z = 0$ . Results are shown for different minimum number of particle per halo,  $n$ . In each panel from bottom to top  $n=25$  (black),  $n=50$  (red),  $n=100$  (green),  $n=200$  (blue) and  $n=400$  (yellow). The particle mass is  $23.42 \times 10^{10} M_\odot$

show in figures 5 and 6 the dependence of  $b_1$  and  $c_2$  on the smoothing radius for several halo minimum masses.

Through all the paper errors on the measured bias parameters have been computed using the jack-knife method with 64 subsamples of the density fluctuations field. This is, we first compute the density fluctuations using the true mean density of the simulation and then we create the jack-knife subsamples from which we obtain, using these fluctuations, a set of 64 bias. Applying equation 20 gives the estimated jack-knife error. We have check that changing the number of regions does not change results significantly.

As expected, we see that the values of  $b_1$  and  $c_2$  change significantly as we increase the smoothing radius  $R_s$  from 5 to  $20 - 25$  Mpc/h, from where they start to converge to their large scale values. The convergence is reached faster at lower mass thresholds and, for a fixed mass, at lower redshifts. In our study we will take an smoothing radius

**Figure 6.** Same as Fig 5 for  $c_2$

of  $30 Mpc/h$  as the one where the convergence regime has been reached. Scatter plots with their fitting curves for this smoothing radius are shown in figures 7 ( $z = 0$  case) and 8 ( $z = 0.5$ ) for different halo mass thresholds. As the mass increases the curve changes its slope and also passes from slightly convex to concave form. This is the change in sign of  $c_2$ . With increasing mass the scatter also becomes more prominent. This is logical since, for a given over density region in the matter field, we are looking for rare objects (more massive halos) and shot noise dominates.

### 5.1 Comparison with the halo model predictions

In figure 9 we show the dependence of  $b_1$  and  $c_2$  on halo mass for both redshifts that we are studying. The results from the scatter relation fits have been plotted in black. We can compare them with the ST predictions for our mass fits (dashed lines) as well as the ST fiducial case  $p = 0.3, q = 0.75$  (dotted lines). We find that the predicted bias generically falls below the local bias from the scatter plot. This happens for all three mass thresholds we use to fit the mass function.

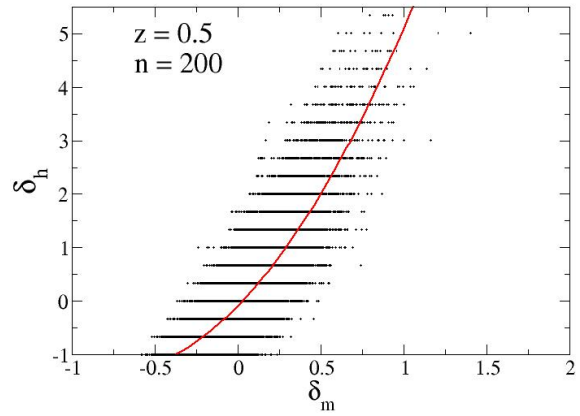
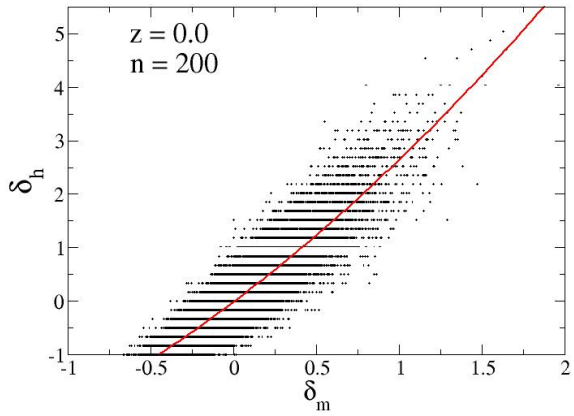
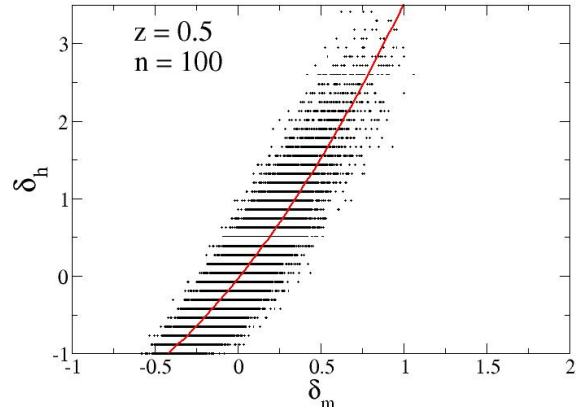
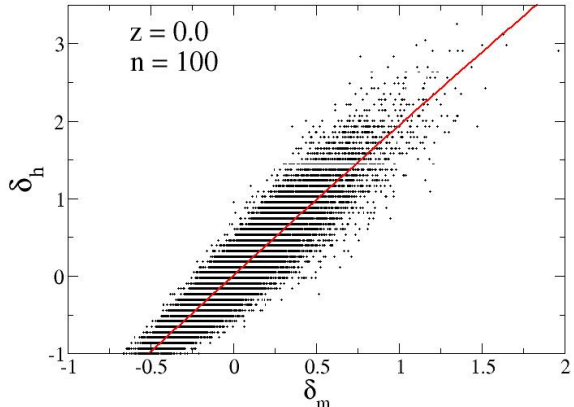
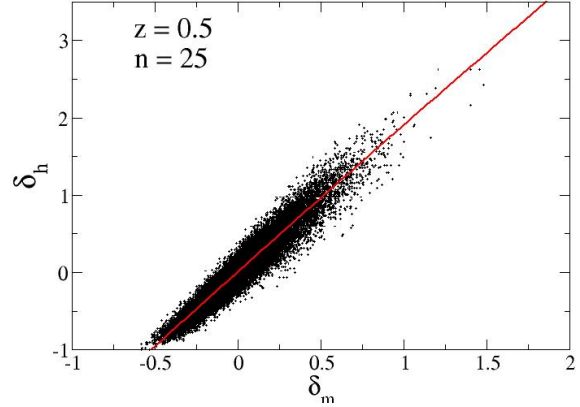
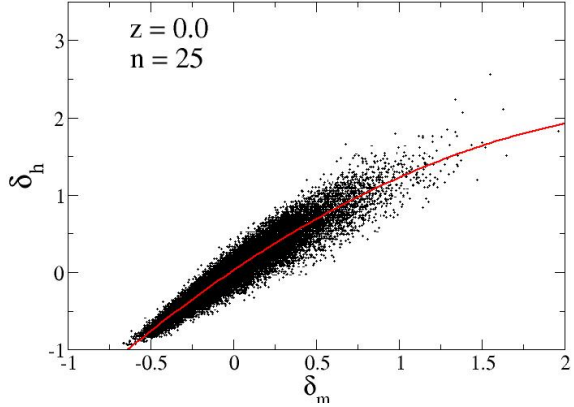


**Figure 7.** Scatter plots showing halo density contrast  $\delta_h$  versus dark matter density fluctuations  $\delta_m$  for a smoothing with  $R_s = 29.8$  Mpc/h. Results from MICE intermediate simulation at  $z=0$ . As labeled, different panels correspond to different minimum number of particles per halo. In a continuous line we show the least square fit to the local bias parabola (equation 9)

**Figure 8.** Same as Fig 7 at  $z = 0.5$

Only for halos above  $7 \cdot 10^{13} M_\odot$  and redshift zero predictions might seem to go above measurements, however, we attribute this to the fact that at this masses we have not completely reach convergence at the smoothing radius we are using, and consequently these points would move a little upwards.

The best agreement between the local bias and the predictions is when the mass function is fitted for masses

above  $10^{14} M_{\odot}$ . The lower the mass threshold to fit the mass function the worst the agreement between measurements and predictions. For a threshold of  $M > 10^{13} M_{\odot}$  predictions are completely misplaced, for a threshold of  $M > 10^{13.5} M_{\odot}$  we have differences of about 5-10%, while if the threshold is  $M > 10^{14} M_{\odot}$  differences are of few percent. This few percent agreement however have to be taken with caution because we are using the high mass halo tail to predict the bias of a halo sample in which most of the halos had not contributed to the ST fit.

In the same plot for comparison we have shown also the predictions for the fiducial ST case of  $p = 0.3$  and  $q = 0.75$ . Its performance is similar to the one with a threshold of  $10^{13.5} M_{\odot}$ , i.e., with differences about 5-10% with the local bias measurement. If we were to use the values  $p = 0.3$  and  $q = 0.707$  that also exist in the literature it would yield much lower values of  $b_1$ , thus we confirm the convenience of using higher values for  $q$  as said in Sheth and Tormen (2001).

In the bottom plot of figure 9 we show the  $c_2$  values from the scatter plot (black dots) against the ST predictions from the mass function fit (dashed lines). As expected  $c_2$  errors from the scatter plot are larger than errors in  $b_1$  since it is more difficult to fit the second order of the Taylor expansion than the first one. For the predictions, statistical errors have been computed using Jack-Knife subsampling (also for  $b_1$ ) but they are not shown because are very small and far less than the systematics we see by changing the mass threshold.

As in the case of  $b_1$  predictions are not very accurate, but they may be useful if one is willing to use bias parameters with errors at 5-10%. Notice that at redshift zero the high mass measured points for the scatterplot may be shifted of order one sigma because of convergence issues. Also one should keep in mind that we are fitting the scatter plot up to the second order, while the ST presumes an expansion to all orders. Thus, our measured bias parameters have a contribution from higher orders comming for the truncation of the Taylor expansion. This may not be important at first order but could be more significant when dealing with  $c_2$ . Added to this, notice that we are fitting the bias parameters using all points of the scatter plot, even those with  $\delta \simeq 1$ . We have checked however that points with  $\delta > 0.5$  are less than 5% of the sample and that excluding them from the fit do not change significatively our results.

In our plots both  $b_1$  and  $c_2$  increase with mass and redshift. Curiously enough the theory predicts a decrease of the parameter  $c_2$  as a function of mass, but for halo masses that are lower than the ones provided by the simulation, so we can not prove this characteristic feature. In the next section we will compare these values of  $b_1$  and  $c_2$  with the ones from clustering measurements. This will allow us to study the accuracy of the halo bias model.

## 6 VARIANCE AND THE SKEWNESS

### 6.1 Variance

One of the common ways of determining the linear bias of galaxies or halos is by comparing their variance with the

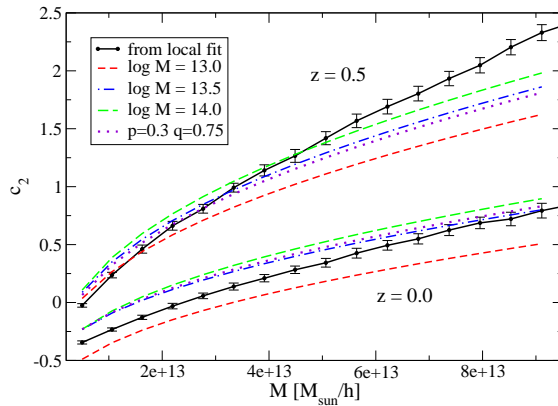
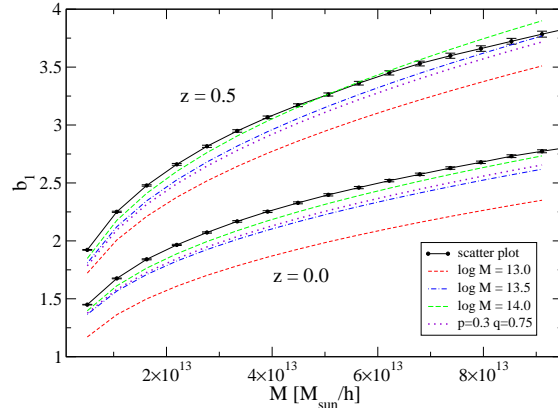


**Figure 9.** Dependence of  $b_1$  (top panel) and  $c_2$  (bottom panel) on the halos mass. In black we show the values measured directly from the  $\delta_h$ - $\delta_m$  local relation in the simulation and compare them with ST predictions (dashed lines) and the fiducial ST  $p=0.3$   $q=0.75$  case (dots). As labeled in the figure each panel have both  $z = 0$  and  $z = 0.5$  results.

measured/predicted matter variance. However, to do the correct comparison one have to account for the shot noise contribution. This contribution to the variance appears because galaxies and halos are not a continuous field, but a discrete one. For a top hat window function,  $W_R(r) = \Theta(|r| - R)$  the poisson shot noise is well known and it is equal to  $1/\bar{n}$  where  $\bar{n}$  is the mean number of halos in a sphere of radius  $R$ . The shot noise corrected variance is therefore:

$$\sigma^2(R) = \langle \delta^2 \rangle - \frac{1}{\bar{n}} \quad (21)$$

where  $R$  stands for the window function smoothing scale. The dark matter in the simulation is also a discrete field and, as mentioned before, it will have its own shot noise correction, which will obviously be much smaller than the halo one due to its higher number density. Now, we can use the halo variance to compute an estimator for the linear bias as

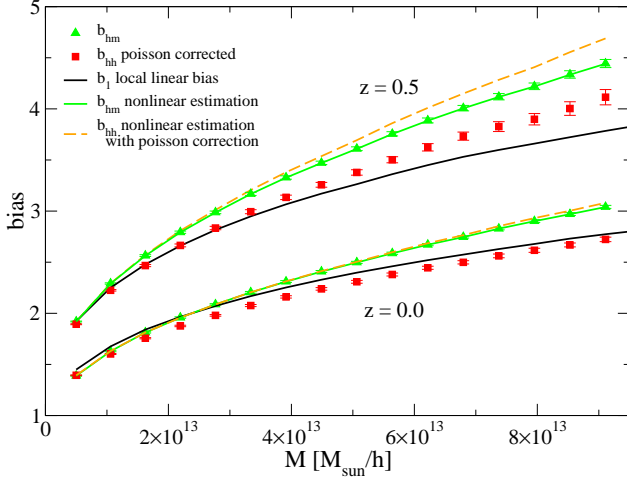


**Figure 10.** Bias a function of halo mass. The linear bias  $b_1$  (shown as black lines) is estimated from a fit to the scatter plot  $\delta_h - \delta_m$  in the simulations, ie from Fig.7-8.. This is compared with the bias values obtained from the (shot-noise corrected) variance  $b_{hh} = \sigma/\sigma_m$  (red squares) and from the cross-correlation  $b_{hm} = \langle \delta_m \delta_h \rangle / \sigma_m^2$  (green triangles). Also shown are the predictions for  $b_{hh}$  and  $b_{hm}$  after applying non-linear contributions (ie in Eq.25 and Eq.26) to the linear bias  $b_1$ . Results are shown for both  $z = 0$  (bottom) and  $z = 0.5$  (on top). Errors are from Jack-knife method with 64 regions

$$b_{hh} \equiv \frac{\sigma(R)}{\sigma_m(R)} = \sqrt{\frac{\langle \delta_h \delta_m \rangle - 1/\bar{n}}{\langle \delta_m \delta_m \rangle}} \quad (22)$$

Another estimator for the linear bias that can be computed from the simulation is

$$b_{hm} \equiv \frac{\langle \delta_h \delta_m \rangle}{\langle \delta_m \delta_m \rangle} \quad (23)$$

In Fig.10 we show the values for the different bias estimators computed in cubical cells of side  $l_c = 48$  Mpc/h. The variance in a cubical cells is very similar to the one in a toptop hat smoothing sphere of equal volume as the cube (Baugh, Gaztanaga & Efstathiou 1995). For our cells of side  $l_c = 48$  Mpc/h the spherical equivalent radius is  $R = 29.8$  Mpc/h. Errors in the figure are from the Jack-knife method with 64 regions, and we have checked that changing the number of regions does not change results significantly.

We can see that all three bias estimators  $b_1$ ,  $b_{hh}$  and  $b_{hm}$  give significative different results given the errorbars. Consequently one needs to be cautious when trying to use these bias estimators for precision cosmology where errors lower than 10% are sought. Below we discuss the origin of these differences focussing mainly in non-linear and discreteness effects. Other contribution could arise from the truncation of the Taylor expansion.

## 6.2 Non-Linear effects

In order to asses how good the linear approximation is we compute the nonlinear contribution to the linear bias  $b_{hm}$

and  $b_{hh}$ . Restricting ourselves to a second order in density fluctuations we have:

$$\delta_h = b_0 + b_1 \delta_m + \frac{1}{2} b_2 \delta_m^2 + \epsilon \quad (24)$$

where  $\epsilon$  is the scatter around the local relation. Because  $\langle \delta_h \rangle = 0$  this sets  $b_0 = -b_2 \sigma_m^2 - \langle \epsilon \rangle$ , and one obtains the following contributions:

$$b_{hm} = \frac{\langle \delta_m \delta_h \rangle}{\langle \delta_m \delta_m \rangle} = b_1 + \frac{1}{2} b_2 S_3 \sigma_m^2 + b_\epsilon \quad (25)$$

where  $b_\epsilon \equiv \frac{\langle \delta_m \delta_\epsilon \rangle}{\langle \delta_m \delta_m \rangle}$ , and  $\delta_\epsilon = \epsilon - \langle \epsilon \rangle$ . Because of symmetry reasons,  $b_\epsilon$  can be expected to be very small, as we will show next.

Nonlinear corrections in equation 25 seem to account very well for the difference that we see in Fig.10 between the measured  $b_{hm}$  (green triangles) and the linear bias  $b_1$  (black continuous line) from the fit to the scatter plots in Fig.7-8. The non-linear correction to  $b_1$  (green line) overlaps well with  $b_{hm}$  measurements within errors. The nonlinear terms are therefore large (10-15% effect) and certainly have to be taken into account in precision cosmology. We infer from this very good agreement that the contribution from the scatter  $b_\epsilon$  in Eq.25 is negligible.

The nonlinear correction for  $b_{hh}$  is:

$$b_{hh}^2 = b_1^2 + \left[ b_1 S_3 + \frac{1}{2} b_2 + \frac{1}{4} b_2 S_4 \sigma_m^2 \right] b_2 \sigma_m^2 + \mathcal{E}_{hh} \quad (26)$$

where the second term include all the non-linear corrections and the third term is:

$$\mathcal{E}_{hh} = b_1 b_\epsilon + \frac{\langle \delta^2 \delta_\epsilon \rangle}{\sigma_m^2} + \frac{\langle \delta_\epsilon^2 \rangle - 1/\bar{n}}{\sigma_m^2} \quad (27)$$

which only includes terms involving the scatter. As pointed out above, because of symmetry, we expect linear terms in  $\delta_\epsilon$  to vanish so that  $\langle \delta_\epsilon \delta_m^n \rangle \simeq 0$ ,  $n = 0, 1, 2$ . This is supported by the agreement of equation 25, with  $b_\epsilon \simeq 0$ , with  $b_{hm}$  measurements shown in Fig.10. The Poisson  $1/\bar{n}$  term comes from the shot-noise correction (ie Eq.22) which allows us to move from the discrete to the continuous halo variance; it assumes a poisson sample of halos in the dark matter field. If the scatter  $\langle \delta_\epsilon^2 \rangle$  in the local relation were truly poisson, then we expect that  $\mathcal{E}_{hh} \simeq \langle \delta_\epsilon^2 \rangle - 1/\bar{n} \simeq 0$ .

In Fig. 10 we find that the non-linear corrections in equation 26 fail to explain the difference between  $b_{hh}$  and  $b_1$ . We find that the predicted  $b_{hh}$  (red dashed line) is higher than  $b_{hm}$  (green triangles) while the measured one (red squares) is lower. In fact, the nonlinear terms seem to increase the differences between the predicted and measured bias. This might be explained if  $\mathcal{E}_{hh}$  turns out to be negative, which could happen if the shot-noise is subpoisson (smaller than poisson) and consequently we are overcorrected shot-noise it by using  $1/\bar{n}$  term. Subpoisson shot noise have been found in simulations (Casas-Miranda et al 2002) for halos larger than  $M_*$ .<sup>2</sup>

<sup>2</sup> Also note that the same effect seems to result in super-poisson errorbars (Cabre & Gaztanaga 2009). This two statements are not in contradiction because the former refers to the Poisson correction to the mean variance (in Fourier or configuration space)

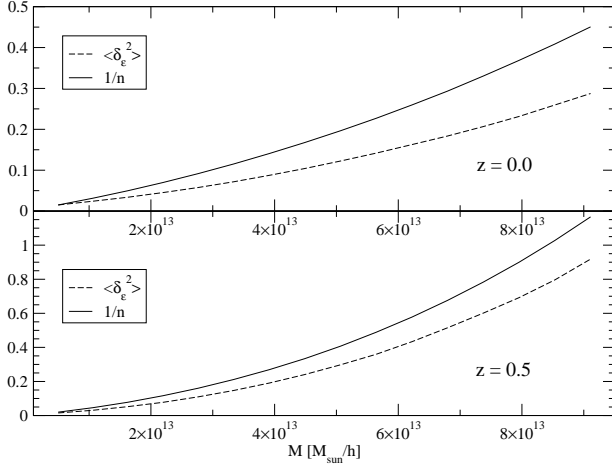


**Figure 11.** Comparison of the poisson shot-noise correction  $1/\bar{n}$  (continuous line) and the scatter  $\langle \delta_e^2 \rangle$  (dashed line) away from the quadratic local bias in Eq.24.

We have indeed found that our halo simulations have  $\langle \delta_e^2 \rangle < 1/\bar{n}$ . This can be seen in Fig.11, which compares the two terms. Besides shot-noise or discreteness effects  $\langle \delta_e^2 \rangle$  also include other sources of scatter: non-local bias and possibly higher order contributions than the quadratic terms in Eq.24. The later is a smoothed component and is unlikely to result in a major increase in the actual scatter. Fig.11 therefore indicates that the combination of non-localities and discreteness produce a variance that is even smaller than the poisson shot-noise.

In Fig.12 we apply the discreteness correction to the prediction rather than to the measurements. When we use the new estimate for the scatter, ie  $\mathcal{E}_{hh} \simeq \langle \delta_e^2 \rangle$  we find a very good match between the predictions and the measurements for  $b_{hh}$ , (this time uncorrected for Poisson shot-noise). We thus see here that, as shown for  $b_{hm}$  in Fig.10, non-linearities are important. But we also note that for the variance we also need a model for the scatter.

### 6.3 Skewness

Another useful clustering statistic for understanding bias is the skewness. As all the moments and cumulants of the halo field it has to be shot-noise corrected. For the normalized skewness this correction is found to be (eg see Gaztanaga 1994):

$$S_3(R) = \frac{\langle \delta^3 \rangle - 3\sigma^2(R)/\bar{n} - 1/\bar{n}^2}{\sigma^2(R)} \quad (28)$$

while the later refers to the noise or error (around the mean 2-point function) induced by discreteness noise.

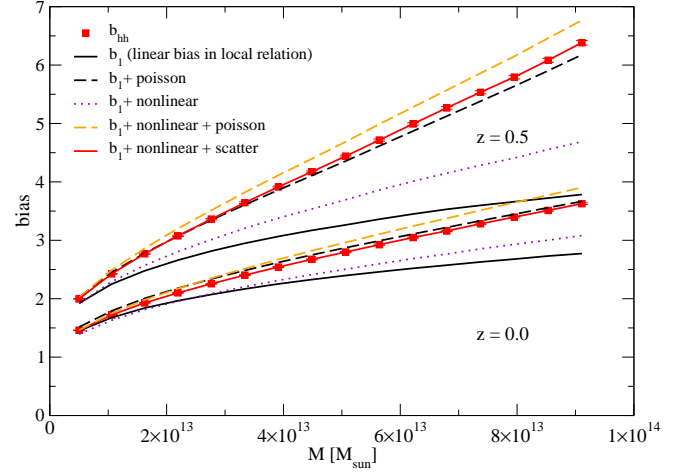


**Figure 12.** Same as Fig. 10, but here we do not apply the poisson shot-noise correction to  $b_{hh}$ . When we apply instead the discreteness correction from measured scatter  $\langle \delta_e^2 \rangle$  (ie see Fig.11) we find a good agreement between the non-linear predictions (red lines) and measurements (red squares).

where  $\sigma^2$  is again the shotnoise corrected variance and  $R$  stands for the window function smoothing scale. Note that when comparing the measured skewness to predictions one has to take into account the fact that we are smoothing the density field. For a top hat smoothing and CDM power spectrum the normalized skewness can be approximated by (Cooray & Sheth 2002; Bernardeau et. al. 2002)

$$S_3 = 4 + \frac{6}{7} \Omega_m^{-2/63} + \gamma_1 \quad (29)$$

where  $\gamma_1 = \frac{d\ln(\sigma^2(R))}{d\ln(R)}$ . Obviously for the Einstein-de-Sitter cosmology and no smoothing we recover the well known value spherical collapse value of  $34/7$ .

With the skewness and the linear bias we can easily compute  $c_2$  as

$$c_2 = (S_3^h b_1 - S_3^m)/3 \quad (30)$$

Here we can either use the direct local  $b_1$  as measured from the  $\delta_h - \delta_m$  scatter plot or other estimators of the linear bias as  $b_{hm}$  or  $b_{hh}$ . Results are shown in figure 13 and compared with the  $c_2$  obtained directly from the  $\delta_m - \delta_h$  scatter plot fit. Errors for these points are computed by means of the Jack-knife method with 64 subsamples in the simulation. Differences between different estimators seems to indicate that, as in the linear case, using only the leading order is not enough, and next-to-leading order contributions as well as modeling stochasticity would be needed for precision cosmology.

### 6.4 Comparison to Halo model

So far we have compared the scatter plot bias values both with ST predictions and with bias from clustering statistics.

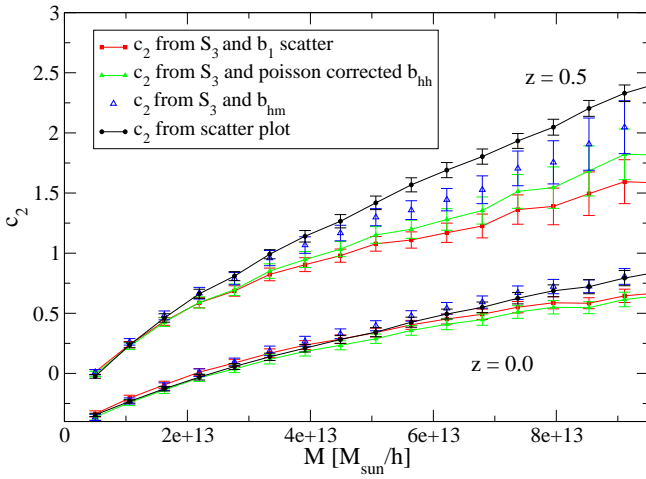


**Figure 13.** Dependence of  $c_2$  on the halos mass as measured directly from the  $\delta_h$ - $\delta_m$  local relation in the simulation (black lines) compared with the values obtained from the skewness and  $b_1$  from the local relation (red lines), from the skewness and  $b_{hh}$  from the halo variance (green lines), and from the skewness and  $b_{hm}$  as predicted in equation 25. As labeled in the figure there are both  $z = 0$  and  $z = 0.5$  results. Errors are from Jack-knife method with 64 regions

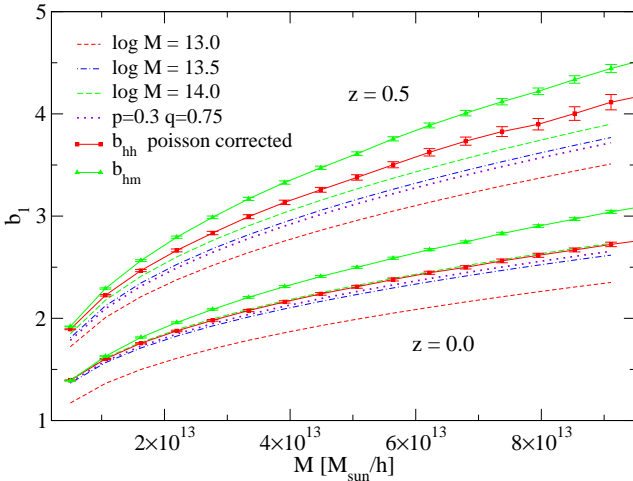


**Figure 14.** Comparison of the linear bias from clustering with ST predictions from the mass function fit. Errors are from Jack-knife method with 64 regions.

Although the scatter plot is useful to study the local bias approximation, it is not a direct observable from surveys. To have a comparison closer to observations we have plot in figures 14 and 15 the bias parameters  $b_1$  and  $c_2$  from clustering statistics with the Sheth and Tormen predictions from a fit of the mass function. Also included for reference is the fiducial ST prediction with  $p = 0.3$  and  $q = 0.75$ . We find that the clustering both  $b_{hm}$  and  $b_{hh}$  are slightly

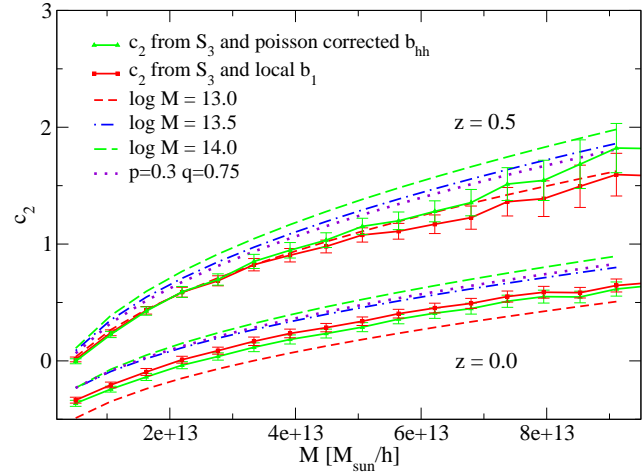


**Figure 15.** Comparison of the bias parameter  $c_2$  from clustering with ST predictions from the mass function fit. Errors are from Jack-knife method with 64 regions

higher than the ST predictions. Similar differences between predictions and measurements were found by Manera et al (2010) when studying the large scale bias from other set of simulations. If we are looking only at the  $b_{hh}$ , ST predictions work at 5-10% level at  $z = 0.5$ . As we will comment in section §10 this could be enough to calibrate mass of halos at about the same percent level. For greater precision more elaborate modeling is needed.

## 7 TWO POINT CORRELATION FUNCTION

We have computed the two point correlation function  $\xi_2(r)$  for the matter and halo density contrast in the simulation. To estimate  $\xi_2(r)$  we have used the  $4\text{Mpc}/h$  density mesh of the simulation and average all the mesh points separated by  $(r \pm \Delta r)$ , where  $\Delta r = 0.5\text{Mpc}/h$ . The results for the matter correlation function and for different halo masses (given by the minimum number of particles per halo) are shown in figure 16. The top panel shows the  $z = 0$  case and the bottom panel the  $z = 0.5$ . To convert particles to halo mass remember that  $M_p = 2.34 \cdot 10^{11} M_\odot/h$ .

As expected the more massive the halos the more biased the correlation function. Note as well what is called the stable clustering, i.e., the fact that for a given halo mass threshold the absolute value of  $\xi_2$  remains approximately constant in redshift while the matter correlation function decreases (in redshift). This could be understood however because halos of a given mass threshold but at different redshift do not correspond to the same Lagrangian mass. The ones at higher redshift are situated in a rarer (less expected) matter fluctuations, being therefore more biased.

The measured correlation function from the simulation shows very clearly the acoustic peak at about  $\sim 110\text{Mpc}/h$  for both the matter and the halo functions. This can be seen in the figure 16. For comparison, in this figure we have also plotted the Linear Perturbation Theory (PT) prediction and

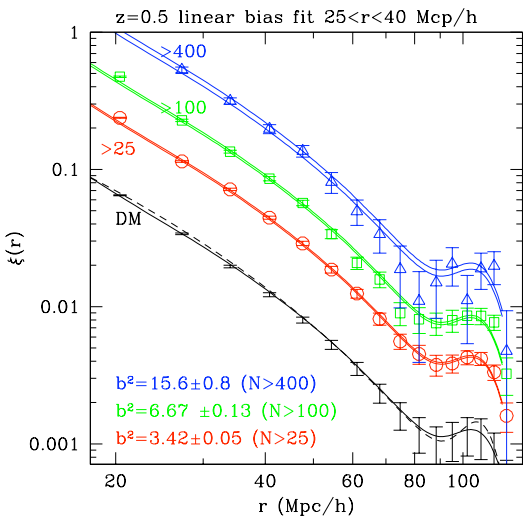
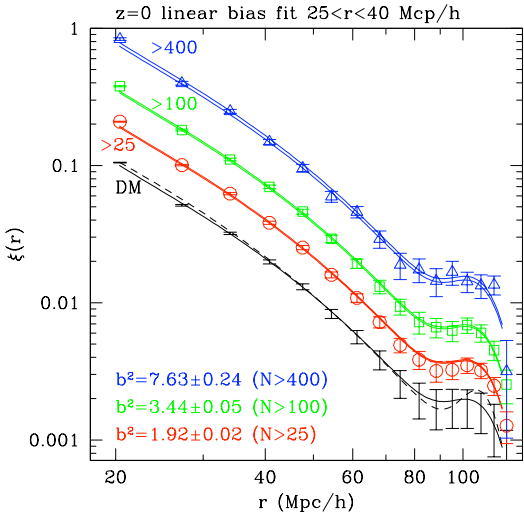


**Figure 16.** Symbols with JK errorbar show the two point correlation function  $\xi_2(r)$  from simulations for different minimum number of particles ( $N > 25, 100$  or  $400$ ) per halo as labeled in the figure. The bottom errorbars corresponds to the measurements in the DM distribution. The bottom continuous (dashed) lines in each panel shows the RPT (linear) theory prediction. The upper continuous lines show the best fit amplitude for the RPT prediction shape, whose amplitudes  $b^2$  are shown in the bottom labels. Top (bottom) panel correspond to  $z=0$  ( $z=0.5$ ).

the Renormalized Perturbation Theory (RPT) prediction for the correlation function, which has been kindly provided by M. Crocce. In the Standard Perturbation Theory PT one expands the equation of motion around their linear solution, assuming that fluctuations are small. The power spectrum can be split into a linear part and higher order correlations. However, for scales approaching the nonlinear regime the truncation at any finite order in PT is not meaningful because neglected higher order contributions are important. The Renormalized Perturbation Theory (Crocce & Scoccimarro 2006; Crocce & Scoccimarro 2006b) gets around this limitation by making a resummation of an infinite subset

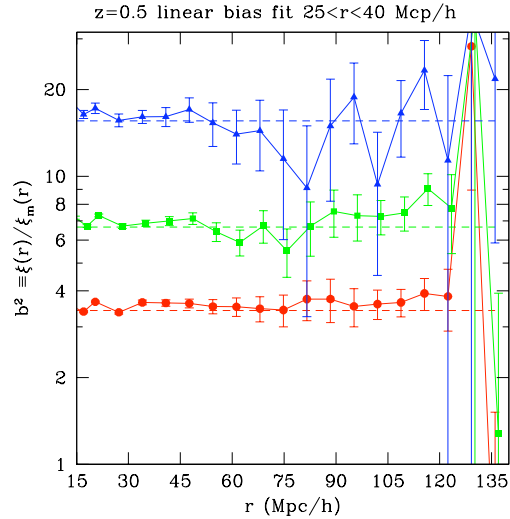
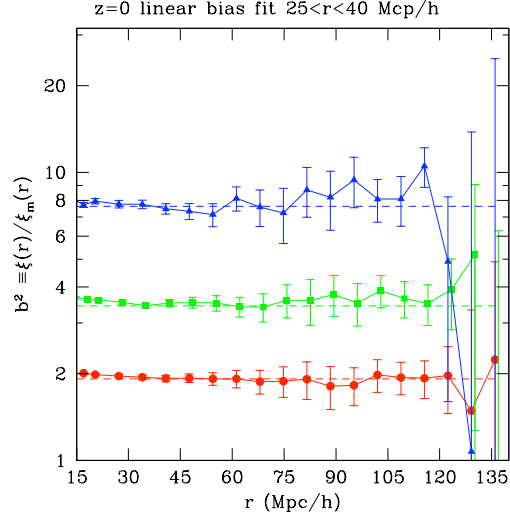


**Figure 17.** Bias from the ratio of two point correlation function  $\xi_2(r)$  for different minimum number of particles per halo  $N=25, 100, 400$  (from bottom to top). Top panel shows results for  $z=0$  and bottom panel for  $z=0.5$ . The dashed lines show the values of the linear bias fit in Fig.16.

of the contributions to the PT expansion. The RPT shows deviations of the linear theory at much larger scales that have been previously thought and already in the acoustic peak scale one gets a contribution of the nonlinear effects. (Crocce & Scoccimarro 2007). As can be seen in the figure these nonlinear contributions results into a smoother prediction for the acoustic peak shape in the RPT than in the standard PT. This seems to be actually in a better agreement with what we find in the simulations.

In this section we are basically interested in measuring the linear bias by comparing the 2-point matter and halo correlation functions. We will then compare these results with the local direct bias determination. For a given lower halo mass threshold we find the bias as

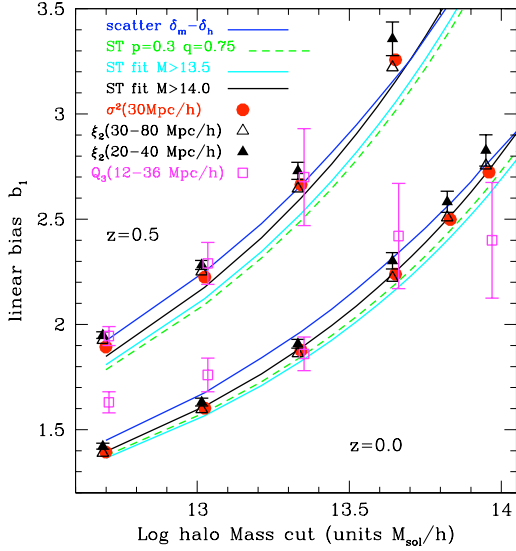


**Figure 18.** Comparison of different estimates for the linear bias. Blue continuous line correspond to the scatter relation in section §5. Rest of the lines correspond to the ST halo model predictions, as labeled in the figure. Closed circle corresponds to the bias from the variance  $b_{hh}$  in section §6.1. Triangles correspond to the ratio of the 2-point function to the RPT predictions on large 30–80 Mpc/h scales (open triangles) and intermediate 20–40 Mpc/h scales (filled triangles). Open squares come from  $Q_3$  in section §7.

$$b(r) = \sqrt{\frac{\xi_2^h(r)}{\xi_2^m(r)}} \quad (31)$$

This bias is expected to be constant at large scales in the local halo model (being the non-constant contribution proportional to  $\xi_2(r)$  and consequently negligible at large  $r$ ). Cosmic variance and shot-noise will add variations to this large scale constant bias. They get more pronounced for larger scales (where we have few modes in the simulation) and for larger halo mass thresholds (since the number of statistics get reduced). This can be seen in Fig.17 where we plot the  $b^2$  for redshifts  $z = 0$  and  $z = 0.5$  and different mass thresholds. We do not find any evidence in the data for scale variations of  $b$  for  $r > 40$  Mpc/h. This favors the local bias approximation, but note that this statement is only accurate within  $\simeq 10\%$  accuracy in our analysis.

We choose to determine the bias  $b$  from the correlation function by fitting the DM measurements of  $\xi_2(r)$  to the RPT prediction. Results are very similar when we use the ratio of halo to DM correlations in Fig.17. In this case, cosmic variance cancels out, but shot-noise introduces large uncertainties for high mass thresholds. We do the fit to RPT for different range of scales. The result is shown as continuous lines in Fig.16 and triangles in Fig.18. We can see in this later figure that, within its errors, these bias estimator is roughly in accordance with the local bias determined directly from the  $\delta_h$ - $\delta_m$  relation or from the cross-variance  $b_{hh}$  in section §6.1. The figure shows how the bias from  $\xi(r)$  are larger when we fit to smaller scales of 20–40 Mpc/h. The ST predictions roughly agree with the other estimates, but this is only true within  $\simeq 5–10\%$  accuracy.

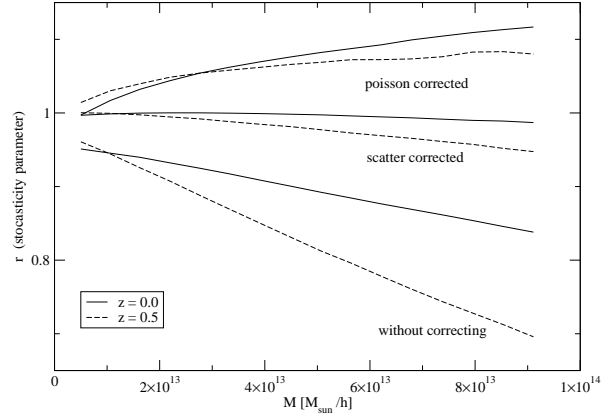


**Figure 19.** Dimensionless cross-correlation coefficient  $r$  in Eq.32 as a function of halo mass. This is for 1-point fluctuations smoothed over cells of  $R \simeq 30$  Mpc/h radius. Different pairs of lines show results using different ways to correct for the discreteness in the halo variance. Dashed (continuous) lines correspond to  $z = 0.5$  ( $z = 0.0$ ).

## 8 GALAXY-MASS CROSS-CORRELATION

A simple measure to study deviations away from the local linear bias relation has been pointed out by several authors ( see Tegmark & Peebles 1998, Dekel & Lahav 1999, and references therein). This is to consider the dimensionless cross-correlation coefficient between the distribution of mass and galaxies (we use halos as a proxy for galaxies in our case):

$$r \equiv \frac{< \delta_m \delta_h >}{\sqrt{< \delta_m \delta_m > < \delta_h \delta_h >}} \quad (32)$$

which is in general a function of scale. In the local linear bias model  $r = 1$ . But both non-linearities and stochasticity (the scatter around the local relation) can change this away from one.

For 1-point smoothed fields we have that in our notation (see section §6.1) this corresponds to:

$$r = \frac{b_{mh}}{b_{hh}} \quad (33)$$

We can estimate this quantity directly from the variance measured in simulations. The result is shown in Fig. 19 as a function of halo mass. We compare measurements using different ways to correct for scatter and discreteness effects in the halo variance: the poisson corrected variance:  $< \delta_h^2 > - 1/\bar{n}$ , the scatter corrected variance  $< \delta_h^2 > - < \delta_\epsilon^2 >$  or the uncorrected variance. The cross-correlation deviates significantly from unity if we do not correct from these effects. Deviations increases with halo mass and redshift, and can be as large as 20–30% for large halos. As shown before (eg see Fig.11) the Poisson model does not provide a good correction for the scatter. If we use instead the scatter away from the local relation measure in the simulation we recover values which are close to unity.

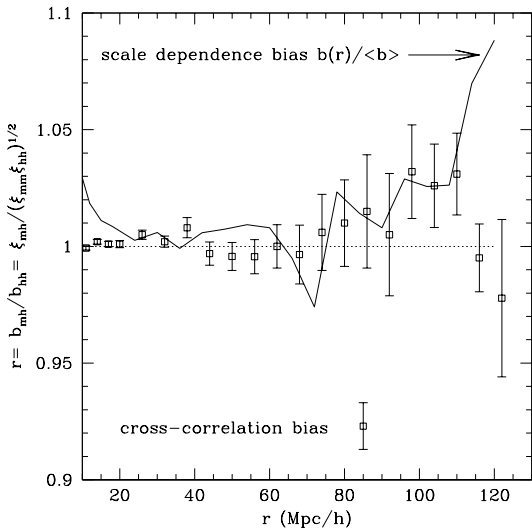


**Figure 20.** Symbols with errorbars show  $r$  in Eq.32, ie the dimensionless cross-correlation coefficient between dark matter and halos with  $M > 5 \times 10^{12}$  in the MICE simulation at  $z = 0.5$ . The continuous line correspond to the scale dependence bias  $b_{hh}$ , normalized to the mean value (ie also shown in Fig.17).

We can also estimate  $r$  in the 2-point correlation function, which should be less affected by discreteness effects. Fig.20 shows  $r$  as a function of scale (separation between pairs) for halos with  $M > 5 \times 10^{12}$ . The measurements are compatible with unity for all scales.

Similar results, but with much larger errors, are found for larger halos masses and different redshifts. Note that for masses larger than  $10^4$  solar masses Manera et al 2010 found  $b_{hm}/b_{hh}$  to be slightly larger than one, being  $b_{hm}$  measured at low  $k$  in Fourier space and  $b_{hh}$  at large separations in the autocorrelation function. In figure 20 we estimate JK errors from the  $r$  ratio, ie we estimate the ratio in different JK subsamples and calculate the error from the scatter in the JK regions (this produces smaller errorbars because sampling variance mostly cancels in doing the ratio).

Altogether, our analysis indicates that the linear local bias model provides a very good approximation, within our sampling errors, for the 2-point function. On scales larger than  $r \simeq 20 \text{ Mpc}/h$ , the halo-halo correlation and halo-mass correlations are, to a good approximation, linear tracers of the underlying dark-matter correlation function and the resulting bias is just the one expected in linear theory. This conclusion is important to interpret measurements of redshift space distortions and BAO in galaxy surveys, which on large scale usually are interpreted under the assumption that linear bias and linear theory are good approximations.

This is not so much the case for the variance, which seems more affected by non-linearities and discreteness effects.

## 9 THREE POINT CORRELATION

We have computed the hierarchical relation  $Q_3(\alpha)$  (see equation 8 ) for dark matter and halos in the simulation. We have used  $r_{23} = 2r_{12} = 24 \text{ Mpc}/h$  and  $r_{13}$  is given by the angle  $\alpha$ . Results for  $z = 0$  ( $z = 0.5$ ) are shown in Fig.21 (Fig.22). Dark matter measurements are shown as (blue) continuous lines while halo measurements and errors correspond to the errorbars. The standard perturbation theory prediction for  $Q_3$  as a dotted line. Notice the characteristic U shape of the hierarchical relation. It is an indication of the dark matter and halo large scale filamentary structure, i.e, aligned structures ( $\alpha \sim 0, \alpha \sim 180 \text{ deg}$  ) are more likely to be found than other configurations (for instance, equilateral triangles).

The values of  $b_1$  recovered from  $Q_3$  (squares) are compared with other estimates in Fig.18. There is good agreement within 1-2 sigma with the general tendency of  $b$  as a function of mass. Again this agreement is only qualitative and there are some significant deviations for small masses ( $\log M < 12.5$ ) at  $z=0$ . There are several possible systematics in this comparison. The PT results (dotted line) is similar but not identical to the DM measurements. The difference is significative and indicates that higher order corrections are needed to match the simulations. We can use this PT prediction, instead of the DM measurements, to fit  $b_1 - c_2$ . The bias estimates are sometimes found to be slightly different. The result also depends on the covariance matrix used in the fit and the number of SV that are included. In general we find that we can fine tune the different ingredients to get better agreement than the one shown in Fig.18, but we do not find this adjustments well justified. For  $z = 0.5$  there seems to be a better agreement than at  $z = 0.5$ . This is not the case at very large masses since errors at  $z = 0.5$  become quite big because of the smaller number density.

## 10 HALO MASS ESTIMATION

We now explore the potential use of linear bias  $b$  measurements to calibrate the mass threshold of a halos sample. For a given mass-bias ( $b$ - $M$ ) relation (eg equation 15 or lines in Fig.18) we can use the measurements of bias  $b$  in the halo sample to predict the corresponding mass threshold. This is illustrated in Fig.23, were we have used the same points as in Fig.18 (for  $z=0.5$ ) and have taken as a model the ST fit to  $\log M > 14$  (which seems to provide the best fit to data) to calibrate mass from bias.

The idea of recovering the mass function from bias and variance measurements, and subsequently fit for cosmological parameters, have been explored by Lima and Hu (2004,2005,2007) in the so-called self calibration method. They assume a peak background split prediction to relate the bias to the mass function ( in particular equation 15 with the fiducial ST values), and allow for an scatter relation between the proxy of the mass (eg X-ray Temperature) and the true mass. Fig. 23 clearly shows that there is a bias (of about 5-10%) in the recovered mass, which will propagate into the cosmological fits as a systematic error. This bias in the recovered mass, could in principle be corrected with the use of mock samples.

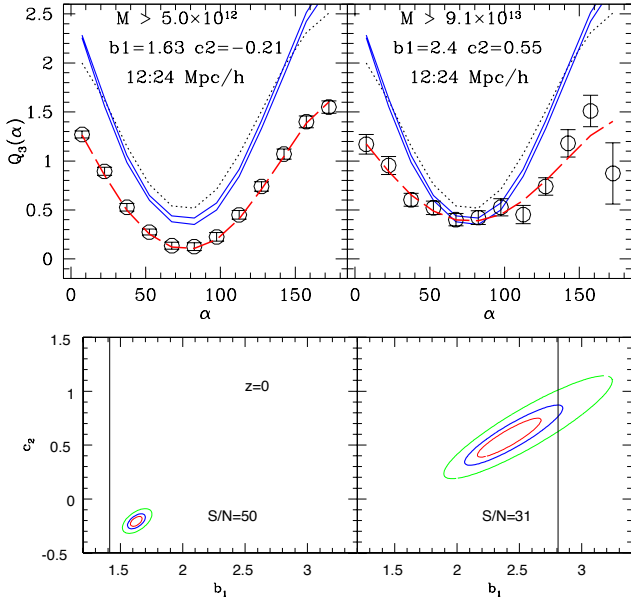


**Figure 21.** Reduced 3-pt function  $Q_3$  for  $z=0$  with  $r_{23} = 2r_{12} = 24$  Mpc/h. Dark matter in the simulation (blue lines encompass the 1-sigma error) as compared to  $Q_3$  in halos (symbols with JK errorbars) of different masses (as labeled). Black dotted lines show the matter PT prediction. Long dashed red lines show the local bias model (equation 10) for the best fit values of  $b_1$  and  $c_2$ . These values are found by comparing  $Q_3$  in halos and in dark matter. Contours in the  $b_1 - c_2$  plane are show in the bottom panels for  $\Delta\chi^2 = 1, 2, 3, 6, 17$ . The vertical lines correspond to the value of the linear bias  $b$  as measured from the ratio of the halo to the dark matter 2-pt function over the same scales.

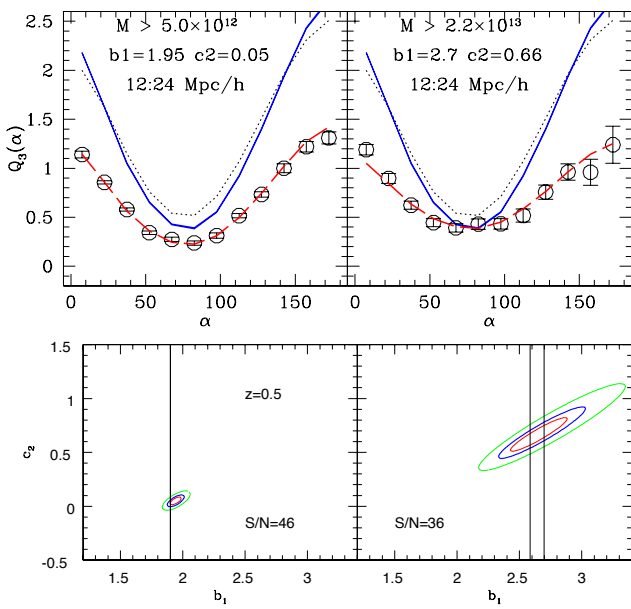


**Figure 22.** Same as Fig.21 for  $z=0.5$

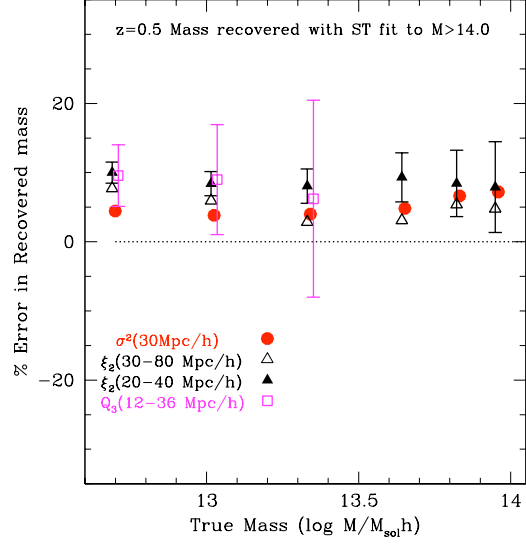


**Figure 23.** Relative error in the Mass recovered using linear bias measurements in Fig.18 together with the bias-Mass relation obtained from ST fit to MF for  $\log M > 14$ . Closed circle corresponds to the bias from the variance  $b_{hh}$  in section §6.1. Triangles correspond to the ratio of the 2-point function to the RPT predictions on large 30-80 Mpc/h scales (open triangles) and intermediate 20-40 Mpc/h scales (filled triangles). Open squares come from  $Q_3$  in section §7.

To measure the bias based on the 2-point statistics we need to know  $\sigma_8$ . Otherwise we just recover the value of  $M$  in units of  $\sigma_8$ . This is not the case for  $Q_3$ , which provides  $M$  with independence of  $\sigma_8$ , but at the expense of a larger errorbar. For large masses there are too few haloes to have a reliable measurement of  $Q_3$ . Also note that observations are in redshift space while here we have only show results in real space. We expect differences in redshift space and we defer this to future studies.

## 11 CONCLUSIONS

In this paper we have used a cosmological dark matter simulation of volume  $V = (1536 \text{ Mpc}/h)^3$  from the MICE simulation team to study the halo clustering and bias of halos above  $10^{13} M_\odot$ . We have looked at the local deterministic biasing prescription, which assumes a local non-linear relation  $T = f(\delta)$  between mass fluctuations,  $\delta$ , and its tracer,  $T$ . We find in the simulations that the local bias is only a crude approximation for halos, with a significant scatter around the mean  $f(\delta)$  relation. We have fitted this scattered relation with a parabola and found the linear bias  $b_1$  and the quadratic bias,  $b_2$  (or equivalently  $c_2 = b_2/b_1$ ) at different smoothings scales (see figures 5 & 6). Constant values are reached for smoothings of  $30 - 40 \text{ Mpc}/h$ .

We have shown that the local bias measurements from the scatterplot parabola and the bias obtained from the halo variance  $b_{hh}^2 = \langle \delta_h^2 \rangle - 1/\bar{n} \rangle / \langle \delta^2 \rangle$  or from the cross variance  $b_{hm} = \langle \delta_h \delta_m \rangle / \langle \delta^2 \rangle$  differ at about 10%, or

even larger for the most massive halos (see figure 10). Differences between  $b_1$  and  $b_{hm}$  can be explained by introducing nonlinear terms, showing that nonlinear contributions are important to be considered when comparing bias. To explain the disagreement between  $b_{hh}$  and  $b_1$  one also have to include the contribution from the scatter in the local relation. We showed that this contribution is smaller than the poisson shot-noise that is costumary to use in the literature.

We have fitted the mass function of halos with a Sheth and Thormen functional form and applyied the peak-background split anstaz to predict the bias parameters. These predictions depend on the mass thereshold used to fit the mass function, being this differences more significant than the errors computed to them using the jack-knife method. Peak-background predictions from the mass function gave systematically lower bias than those measured from clustering, i.e,  $b_{hh}$  and  $b_{hm}$  at about 5-10% (see figures 12-13) and do match the bias parameters from the local scatter plot only at about the same level of precision (see figure 9).

We have measured the correlation function of halos,  $\xi_h(r)$ . By fitting it on scales of  $30-80\,Mpc/h$  and comparing it to the matter correlation funcion we have find the correlation bias, which is aproximately constant at large scales (see figures 14-15), although there is some room for a small scale dependence at scales near the BAO. Fitting the correlation function at smaller scales  $20-40\,Mpc/h$  gives a slightly larger bias. We have also used three point function measurements to obtain  $b_1$  and  $b_2$ .

Most of the linear bias values of this paper are summarized in figure 16. We see that in many cases they agree at 5-10% level. More work should be done to narrow this to at order percent level that will be likely needed in future surveys to constraint cosmology and learn about galaxy formation. Our work is pointing towards the necessity including non-linear and possible non-local terms when comparing different bias estimators. We are planning to work in these lines.

Finally, we have estimated the mass of halos from the measured bias (figure 19), showing that there is a systematic error when using the common ST peak-background split prediction. These systematic errors have to be taken into account when recovering the mass function from clustering of halos, since they will propagate to the estimator of cosmological parameters, like the dark energy equation of state.

## ACKNOWLEDGMENTS

We thank all the MICE collaboration team, and specially P. Fosalba who provided the central positions of halos in the simulation. We thank Roman Scoccimarro for his comments on the first draft of this paper. This work was partially supported by NSF AST-0607747, NASA NNG06GH21G and NSF AST-0908241, and by the Spanish Ministerio de Ciencia y Tecnologia (MEC), projects AYA2009-13936-C06-01 and Consolider-Ingenio CSD2007-00060, and research project 2009SGR00728 from Generalitat de Catalunya. MM acknowledge support also from the DURSI department of the Generalitat de Catalunya, the European Social Fund.

## REFERENCES

Barriga J., Gaztanaga E., 2002, MNRAS 361, 842  
 Baugh, Gaztanaga & Efstathiou 1995, MNRAS 274, 1049  
 Bernardeau F., Colombi S., Gaztanaga E., Scoccimarro R., 2002, Phys. Rep. 367, 1  
 M. J. I. Brown, Z. Zheng, M. White, A. Dey, B. T. Jannuzzi, A. J. Benson, K. Brand, M. Brodwin, D. J. Croton, 2008, ApJ.  
 Dekel, A & Lahav O., 1999, ApJ 520, Issue 1, p22-34  
 Casas-Miranda R., Mo H.J. Sheth R.K., Borner G., 2002, MNRAS 333, 730-738  
 Cole S., Kaiser N., MNRAS 237 (1989) 1127  
 Cooray A. & Sheth, 2002, Phys. Rept. 372, 1-129  
 Crocce M., & Scoccimarro R., 2006, PRD 73, 063519  
 Crocce M., & Scoccimarro R., 2006, PRD 73, 063520  
 Crocce M., & Scoccimarro R., 2007,astro-ph 070427, submitted to PRD  
 Crocce, M., Fosalba, P., Castander, F. J.; Gaztanaga, E., 2009, eprint arXiv:0907.0019  
 Feldman H.A., Frieman J.A., Fry J.N. & Scoccimarro R., 201, PRL 86, 1434  
 Frieman J.A., & Gaztanaga E., 1994, ApJ 425, 392-402  
 Fosalba P., Gaztañaga E., Castander F. J., Manera M., 2008, MNRAS, 391, 435  
 Fry J.N., 1984, ApJ 279, 499  
 Fry J.N., & Gaztanaga E., 1993, ApJ, 413, 447  
 Gaztanaga E., Scoccimarro R., 2005, MNRAS 361, 824-836  
 Gaztanaga E., Norber P., Baugh C.M., Croton D.J., 2005, MNRAS 364, 620-634  
 Eke, V. R., Cole, S., Frenk, C. S. 1996, MNRAS, 282, 263  
 Lima M. & Hu W. 2007, PRD 76, Issue 12, 123013  
 Lima M. & Hu W. 2005, PRD 72, Issue 4, 043006  
 Lima M. & Hu W. 2004, PRD 70, Issue 4, 043504  
 Manera M. Sheth R.K., Scoccimarro R., 2010, MNRAS 402, 589-602  
 Martino M.C., Sheth R.K., 2009, MNRAS, 394, 2109  
 Peebles P.J.E., 1980, The Large-Scale Structure of the Universe. Princeton Univ. Press, Princeton, NJ  
 Press W. & Schechter P., 1974, Astrophys. J., 304, 297  
 Sefussati E., Scoccimarro R., 2005, PRD 71, Issue 6, 063001  
 Sheth R.K. & Tormen G., 1999, MNRAS, 301,119  
 Sheth R.K. & Tormen G., 2001, MNRAS, 323,1  
 Scoccimarro R., Couchman H.M.P., & Friedman J.A., 1999, ApJ 517, 531-540  
 Scoccimarro R., Sheth. R.K., Hui L., Jain B., 2001, ApJ 546, 20  
 Tegmark, M. & Peebles, J, ApJ 500, L79  
 J.L. Tinker, D.H. Weinberg, Z. Zheng (2006) Mon.Not.Roy.Astron.Soc. 368, 85-108  
 J.L. Tinker, A.R. Wetzel, (2009) eprint arXiv:0909.1325  
 Warren M.S., Abazajian K., Holz D.E., Teodoro L., ApJ 2006, 881  
 Z. Zheng, I. Zehavi, D.J. Eisenstein, D.H. Weinberg, Y.P. Jing (2009) accepted in ApJ, eprint arXiv:0809.186  
 Z. Zheng, A.A. Berlind, D. H. Weinberg, Astrophys.J.633:791-809,2005